



RESEARCH ARTICLE

10.1029/2018JD028732

Key Points:

- A 2.5-m telescope at midlatitudes is employed for high-resolution observations of the OH layer
- Quasi periodic structures on scales between 60 and 4.5 m were observed
- Observed structures follow a Kolmogorov type model of turbulence with a $-5/3$ power law

Correspondence to:

C. Franzen,
christoph.franzen@ntnu.no

Citation:

Franzen, C., Espy, P. J., Hibbins, R. E., & Djupvik, A. A. (2018). Observation of quasi-periodic structures in the hydroxyl airglow on scales below 100 m. *Journal of Geophysical Research: Atmospheres*, 123, 10,935–10,942. <https://doi.org/10.1029/2018JD028732>

Received 28 MAR 2018

Accepted 21 SEP 2018

Accepted article online 24 SEP 2018

Published online 8 OCT 2018

©2018. The Authors.

This is an open access article under the terms of the Creative Commons Attribution-NonCommercial-NoDerivs License, which permits use and distribution in any medium, provided the original work is properly cited, the use is non-commercial and no modifications or adaptations are made.

Observation of Quasiperiodic Structures in the Hydroxyl Airglow on Scales Below 100 m

Christoph Franzen^{1,2} , Patrick Joseph Espy^{1,2} , Robert Edward Hibbins^{1,2} , and Anlaug Amanda Djupvik³

¹Department of Physics, Norwegian University of Science and Technology (NTNU), Trondheim, Norway, ²Birkeland Centre for Space Science, Bergen, Norway, ³Nordic Optical Telescope, Santa Cruz De La Palma, Spain

Abstract Gravity waves are known to transport energy and momentum to the middle atmosphere. The breaking processes associated with divergence of fluxes of energy and momentum into the atmosphere occur on scales that cannot be resolved in models and therefore have to be parameterized. The question remains as to whether it is possible to use a turbulence model on scales below 100 m and what kind of turbulence model should that be. Here we use high spatial resolution observations of the OH nightglow located near 90-km altitude from the Nordic Optical Telescope to observe quasiperiodic structures down to horizontal scales of 4.5 m. These results indicate that a Kolmogorov type of energy cascade model of turbulence with a $-5/3$ power law appears to be satisfied down to these short, 4.5-m scales.

1. Introduction

1.1. Gravity Wave Breaking

Gravity waves propagating upward from the lower atmosphere transport energy and momentum into the upper atmosphere. As they propagate upward their amplitudes grow to conserve energy as the background density decreases with altitude. Ultimately, wave-induced temperature gradients exceed the adiabatic lapse rate (Holton, 1982; Lindzen, 1981). When this occurs, the waves begin breaking, dissipating energy and depositing momentum into the surrounding atmosphere (Staquet & Sommeria, 2002). There are also other breaking mechanisms that can lead to instabilities, including self-accelerating instabilities (Fritts et al., 2015), wave-induced shears, or wind-induced critical levels, where the intrinsic wave speed approaches that of the wind (Fritts & Alexander, 2003). These breaking processes generally take place in the mesosphere and lower thermosphere (MLT), where this wave momentum drives the mean flow away from radiative equilibrium and produces a pole-to-pole meridional circulation in the MLT (Holton, 1983).

The intensity of the terrestrial airglow layer, produced at night by chemiluminescent reactions associated with the recombination of atomic species that have been photodissociated during the day, is modulated by the temperature and density perturbations associated with these gravity waves as they pass through the layer. The hydroxyl (OH) airglow near 90 km (Meinel, 1950a, 1950b) is one of the more intense emissions, and observations of the OH airglow are often employed to measure gravity waves and breaking features in the MLT region (Dietrich et al., 2005; Fritts et al., 2017; Li et al., 2005). Responding to a wide range of vertical wavelengths (Liu & Swenson, 2003; Swenson & Gardner, 1998), measurements of the horizontal wavelength of gravity waves have been made with OH airglow imagers (Sedlak et al., 2016; Taylor et al., 2007). Studies such as these typically detected atmospheric gravity waves in the OH airglow layer on scales of the order ~ 1 to hundreds of kilometers. Other studies (Dewan et al., 1992; Fritts et al., 2017; Hecht et al., 1997) have observed turbulent and wave-breaking features in the OH layer on scales larger than a kilometer and with frequencies up to 0.01 Hz.

During the breaking process, the waves do not instantaneously deposit all their energy. Rather smaller and smaller structures are created with ever increasing wave numbers in the process (Becker & Schmitz, 2002). These smaller-scale structures, including secondary waves and turbulence, can have a phase direction different from that of the primary wave (Fritts et al., 2017) and carry less energy. Kolmogorov (1941a, 1941b) described this cascade-breaking process with a simple diffusion model, where the energy cascades as a $-5/3$ power law with the wave number of the wave like structure. While some measurements of the OH airglow have observed such a $-5/3$ power law for kilometer-scale waves (Dewan et al., 1992; Hecht et al., 2005),

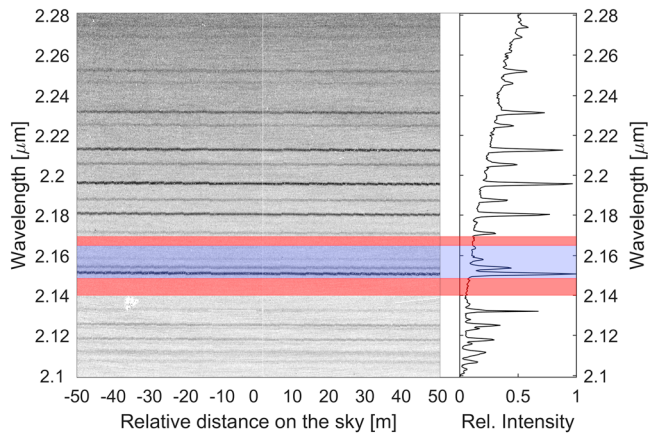


Figure 1. Example of one integration from May 2016. The integration time is 20 s. Only the (9,7) transition is shown with P, Q, and R branch from top to bottom. The left side shows the spatially resolved picture along the slit over 100 m of sky at the OH layers' mean altitude. The right side shows the accumulated spectrum over the whole slit. The blue area marks the Q branch, while the red areas mark pure background noise areas on both sides of the Q branch.

it is unclear whether this turbulence model can be assumed at the smallest, parameterized scales below 100 m to characterize this energy transfer.

In this paper we will present measurements on the OH airglow Q branch of the (9,7) transition at 2,100 nm to 2,250 nm. These measurements have been made using the NOTCam spectrograph mounted on the Nordic Optical Telescope (NOT) in La Palma. The high throughput of the system coupled with its high temporal resolution (~ 10 s) affords the opportunity to utilize the high spatial resolution along the slit (10 cm/pixel) to measure quasiperiodic structures (QPS) in the OH with horizontal wavelengths below 100 m. The energy cascade of these small-scale structures complements previous studies at larger scales and adds to a further understanding of the energy deposition of gravity waves in the MLT.

1.2. Instrumentation and Data

The measurements presented in this paper were taken with the NOT. The NOT is part of the Spanish Observatorio del Roque de los Muchachos, situated in La Palma, Canary Islands, Spain ($17^{\circ}53'$ W, $28^{\circ}45'$ N). The telescope has an f/2 primary mirror with a diameter of 2,560 mm (Djupvik & Andersen, 2010). The spectroscopic instrument used here is the NOT near-infrared Camera and spectrograph (NOTCam). The detector is a

$1,024 \times 1,024$ pixel Rockwell Science Center HgCdTe "HAWAII" array. The slit size is 50 mm by 0.128 mm, with a field of view of 4 arc min by 0.6 arcsec. Taking the altitude of the OH layer to be 87 km (Baker & Stair, 1988), this projects to a spatial area of 100 by 0.25 m on the OH airglow. Therefore, effects across the slit width are neglected in this work. The filter used here is a K' bandpass filter for wavelengths between 1,950 nm and 2,290 nm. Both the (9,7) and the (8,6) transitions can be found in this wavelength region. The resolving power used, $R = \lambda/\Delta\lambda \sim 2,100$, is sufficient to separate the R, Q, and P branches, as well as to resolve or partially resolve the individual rotational lines in each branch, as shown in Figure 1.

Data were obtained for two, approximately 1-hr-long observing periods on both 21 May 2016 and 20 June 2016 without automated star tracking. Instead, the telescope was pointed to the zenith in a staring mode and away from the galactic plane with the slit length orientated perpendicular to the apparent movement of the stars in the sky. That is, the slit was oriented on the north-south axis. In this orientation, stars pass through the 0.6 arcsec field of view of the slit width in 0.04 s, minimizing their effects on the background. For each hour of observation, spectra were recorded using an integration time of 20 s (21 May) or 10.8 s (20 June). After each integration there was a dead time of about 12 s during which time the detector was read out. Table 1 below summarizes the observations.

Figure 1 below is a typical example of a single 20-s integration recorded during May that shows only the (9,7) transition of OH and describes the techniques used to process the data. The basic data processing for telescope data of the OH is described in Franzen et al. (2017). Briefly, the effects of the known bad pixels on the detector and the curvature of the image due to focal plane orientation were corrected. Similarly, a dark image was used to remove detector background, and the relative spectral sensitivity was corrected using a 3200 K deuterium lamp as a flat field calibrator right before or after the observations.

Shown on the left side of the figure is the detector image with the horizontal axis showing distance along the slit length, mapped to the nominal 87-km altitude of the OH layer (Baker & Stair, 1988). The vertical axis is the spectral axis labeled in wavelength. The image grayscale is inverted, and the individual OH spectral lines in emission are therefore seen as the black horizontal lines in the image.

On the right side of Figure 1, the spectrum is integrated along the horizontal, slit-length axis to show the total intensity as a function of wavelength. The spectrum is presented in uncorrected relative intensity for simplicity.

Table 1
Technical Details of the Observations

Date of observation	21 May 2016	20 June 2016
Integration time (s)	20	10.8
Repetition time (s)	32	24
# of integrations	133	167
Total time (min)	71	67
Time (UT)	22:07–23:18	22:23–23:30

Note. Shown are the dates of the observation, the integration times, the total repetition time between each two integrations (integration time plus read-out time), the total number of integrations executed, and the total time of the whole observation, as well as the UT time of the observations.

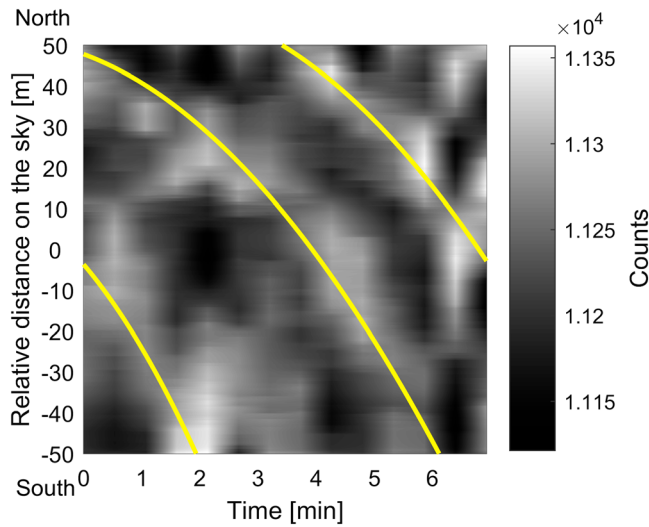


Figure 2. Example keogram of a quasiperiodic structures (QPS) event across 100 m of sky. The display lasted from minute 31 to minute 38 of the observation from 21 May 2016. The integration time per time step is 20 s. Three QPS crests are visible over the course of about 7 min, moving to the right of the picture. The QPS crests' positions are highlighted in yellow by a polynomial fit of second order through the maximum values along the three crests. The observed wavelength is around 30–40 m. The intensity color scale is in counts.

The blue area marks the Q branch in the center of the (9,7) transition. The two red areas on either side mark areas of background noise free of OH lines. The P branch can be seen at longer wavelengths, while the R branch is visible at shorter wavelengths.

2. Method

The spectrum on the right side of Figure 1 shows the sum over all 1,024 pixels along the slit of the telescope. However, each column of pixels from the left side of Figure 1 shows the spectrum for each 10-cm-wide position on the sky along the slit length. A variation across the observed 100 m of sky will therefore be visible as a change in the intensity of the spectrum between these columns.

There is an underlying background in the spectra presented in Figure 1 that is obvious in the integrated spectrum on the right. To remove this, the background level on either side of the Q branch is measured, and the background below the lines of the Q branch is approximated by linear interpolation and then subtracted. Then, the signal across the Q branch from 2,148.5 to 2,165 nm is integrated for each column to obtain the total intensity of this branch, independent of the rotational temperature, for each spatial element along the slit length. A 10-pixel median filter, which represents 1 m at the OH altitude, is applied to the integrated Q branch along the slit columns to increase the signal-to-noise ratio and avoid aliasing in the subsequent analysis.

This procedure is employed on each 10- or 20-s data sample, yielding the time evolution of the Q branch intensity at every spatial location along the slit. The temporal sequence is combined to form a keogram (Eather et al., 1976), an example of which is presented in Figure 2. The figure shows the intensity along the slit for each time along the horizontal axis with intensities shown by the color scale. Three bright lines of high intensities (highlighted in the figure by a simple polynomial fit of second order through the maximum values of each of the three crests) are visible, indicating three QPS crests moving to the south over the course of 7 minutes. The wavelength of the QPS shown is about 30–40 m, with small variations. If the orientation of the structure is at an angle φ relative to the slit direction, this wavelength would be longer by a factor $1/\cos\varphi$ than its true wavelength. A discussion of the implications of this projected wavelength compared to the real wavelength will be given later in the paper.

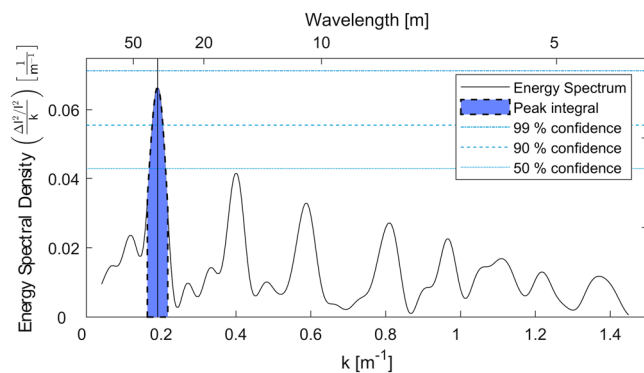


Figure 3. Lomb-Scargle periodogram of one time step from around the middle of the example event presented in Figure 2. The clear peak around the wave number 0.19 m^{-1} (corresponding to a 33-m horizontal wavelength) is marked by the black vertical line. The integral over the peak is shown in blue. Other, smaller peaks show events whose durations were less than one Brunt period and are therefore not counted as an event. The blue horizontal lines show the lines of 50%, 90%, and 99% confidence in dotted, dashed, and dash-dotted, respectively.

In order to quantitatively extract even weak structures and their temporal duration, we present a method based the work of Humberst et al. (2017). As detailed below, the method uses a Fourier-based technique to separate the spatial frequencies present and a correlation between the temporal samples to determine their duration. The example of QPS presented here in Figure 2 will serve as the example through the steps of the procedure.

We employ a Lomb-Scargle algorithm (Lomb, 1976; Scargle, 1982) along the slit length, which yields the energy spectral density per spatial-frequency interval at each temporal sample. As an example, a time step from the middle (at about 4.3 min into the keogram presented in Figure 2) is used as input data to the Lomb-Scargle algorithm. The resulting energy spectral density is shown in Figure 3. If random noise in the data has a probability, p_o , of creating a spectral estimate of amplitude z_o , then the level of confidence, $(1 - p_o)$, with which one can eliminate the hypothesis that random noise in the data created a spectral amplitude z_o is given by

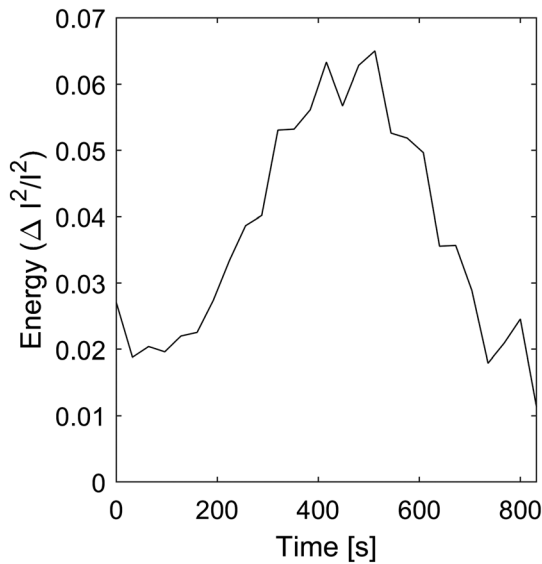


Figure 4. Temporal evolution of the energy of the QPS (spectral density integrated over the full width at half maximum wave number bin between 0.16 m^{-1} and 0.22 m^{-1}) for the data presented in Figure 2. This shows the fluctuation to be an isolated event, with a duration of approximately 600 s.

$$z_0 = -\ln \left[1 - (1 - p_0)^{\frac{1}{N}} \right],$$

where N is the number of data points (Scargle (1982)). The blue horizontal lines in Figure 3 represent the spectral amplitudes where random noise can be excluded as the source with 50%, 90%, and 99% confidence, shown as dotted, dashed, and dash-dotted lines, respectively. The highest peak in the spectrum, significant above the 90% confidence level, appears at radial wave number $k = 2\pi/\lambda = 0.19 \text{ m}^{-1}$ (or 33 m wavelength). This corresponds to the approximate distance between QPS crests that can be seen in Figure 2. The relative energy in the peak is taken to be the integral over the peak's full width at half maximum, 0.06 m^{-1} , which is set by the total distance spanned by the slit length.

This integral over the peak is executed for the Lomb-Scargle periodogram of each individual time sample. Regions of significant (at the 50% confidence level) energy spectral density at wavelengths that are coherent over time indicate an event rather than random fluctuations. While a 50% confidence level on an individual spectrum is relatively low but tolerable (Vetterling et al., 1992), we require a peak to be above the 50% level over at least a full Brunt period. This means that the peak would occur at or above the 50% confidence level at least 10 times in a row, allowing one to say that at the 99.9% confidence level, random noise in the data is not responsible for this peak.

For example, for the data presented in Figures 2 and 3, the temporal evolution of the energy (the spectral density integrated over the full width at half maximum wave number bin between 0.16 m^{-1} and 0.22 m^{-1}) is shown in Figure 4. The data in the Figure have been smoothed with a 1.5-min running median filter, and the event is visible for a duration of about 600 s.

To determine which events show coherent behavior in time and to get a consistent, quantitative measure of the length of the event, we use the autocorrelation function of the temporal evolution of energy shown in Figure 4. An event with constant energy with abrupt starting and ending times would have a triangular lagged-autocorrelation function centered at zero lag with a maximum value of 1. The lag at which the autocorrelation passes 0.5 in the positive and negative directions represents the length of the event.

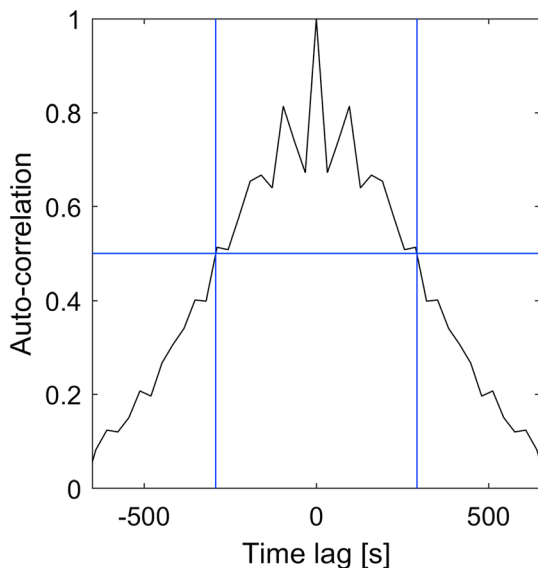


Figure 5. Lagged autocorrelation of the data presented in Figure 2 in the integrated spectral density bin between 0.16 m^{-1} and 0.22 m^{-1} . The point of 0.5 correlation is highlighted with blue lines for both positive and negative lags. The lag at these points is $\pm 288 \text{ s}$, which yields an event length of 576 s. This is consistent with the qualitative evaluation from Figure 4.

Figure 5 shows the autocorrelation of the example data discussed above. The triangular structure is clearly visible and the points measured at a correlation greater than 0.5 yield an event length of 576 s, which agrees with the qualitative observation in Figure 4 of about 600 s. Events with a duration shorter than one Brunt period, which is roughly 300 s for the atmospheric conditions during the experiments presented here, are attributed to noise.

To treat the entire data set, a Lomb-Scargle periodogram is created for the spatial distribution along the slit length, as described above, for each temporal sample during the night. For each of these resulting periodograms, the wave numbers of peaks with significance $\geq 50\%$ level, as well as their corresponding energies (the integral over the full width at half maximum) and time, are recorded. Taking each peak separately, the time sample when a significant peak first occurs is taken as the starting point, and the time series of energy versus time at that peak position is formed for all consecutive time samples, where the peak remains significant at $\geq 50\%$ level. The resulting time series of energy is then autocorrelated as shown on the example in Figure 5. A peak whose energy autocorrelation

consistently remains above 0.5 for a duration longer than a Brunt period is taken to be a QPS. The process is repeated for all peaks found to be significant at $\geq 50\%$ level.

While QPS may occur with durations shorter than a Brunt period, we have limited our analysis to events with duration of at least one period. This corresponds to about 300 s for the atmospheric conditions during our observations, and requires the peak in the power spectrum to be at the 50% significance level in at least 10 consecutive scans. The choice of 50% as the minimum criterion for significance in a single periodogram allows us to exclude random noise as the cause of the peak at an overall confidence level of 99.9%. However, this does not imply that QPS of duration shorter than one whole Brunt period may not occur.

3. Results and Discussion

We employ the method presented in the previous section on the observations from both nights. The first observation from 21 May yields 22 consistent QPS events. The second observation from 20 June yields 20 events. Together these 42 QPS events cover a time span of about 140 min. All the events span the wave number range from 0.11 m^{-1} (a 60 m wavelength) to 1.39 m^{-1} (4.5 m wavelength), which substantially expands the range of QPS features that have been observed in the OH airglow.

Figure 6 below gives an overview over the 42 QPS events found. Figure 6a presents the events for the observations from 21 May 2016, while Figure 6b shows the results for the observations from 20 June 2016. Each box represents one event, with the horizontal length showing the timespan over which the QPS could be observed. The QPS events range between 300 and 1,100-s length, with an average of 490 s. The vertical width of the box shows the full width at half maximum of the observed wave number peak from the Lomb-Scargle periodogram. The wavelengths corresponding to the wave numbers are indicated on the axis on the right-hand side. The darkness of the box indicates the relative energy of the event. A darker shade of gray represents a higher energy. It is apparent that events at smaller wave numbers have higher energy than those at larger wave numbers.

Figure 7 shows a log-log plot of the relative energy (in $\Delta I^2/I^2$) versus observed wave number for the events from the two nights of observations shown in Figure 6. The linear trend on the log-log plot indicates a power law relation between energy and wave number. The red line shows a power law fit that yields an exponent of -1.62 ± 0.08 , with a correlation coefficient of -0.95 . This value agrees to within one sigma with the $-5/3$ relation that would be expected from a Kolmogorov model of turbulent cascade (Kolmogorov, 1941a, 1941b). This suggests that the relationship holds for the QPS fluctuations found in the OH layer with wave numbers between 0.11 m^{-1} and 1.39 m^{-1} (wavelengths between 60 and 4.5 m). Previous workers (Cot, 2001; Dewan et al., 1992; Hecht et al., 1994) have found similar exponential relationships between QPS energy and wave number for QPS with kilometer scales. The results presented here suggest that the energy decay during breaking continues down to wave numbers as small as 1.39 m^{-1} (4.5 m wavelength), indicating that a Kolmogorov type model can be used to describe the turbulent cascade of energy in the MLT down to meter scales.

While the energy and the wave number show a clear correlation, the duration of the events is not correlated to either the energy or the wave number. That means that longer duration events show no tendency to have more or less energy than shorter ones, and that QPS events with higher wave numbers have no tendency to last longer or shorter than waves with smaller wave numbers.

The observations presented here, as with any measurement, have their own biases. For one, we observe only QPS with a well-defined wavelength structure and not random turbulent fluctuations. For another, we observe these structures in the horizontal, not the vertical. Finally, we have no altitude information as to where in the OH layer these structures may occur. Rocket observations near 90 km of the continuum of turbulent fluctuations in the vertical have reported the break to the dissipative region between 10 and 40 m (Hillert et al., 1994; Lübken, 1992; Lübken et al., 1994, 2002; Müllemann et al., 2002; Thrane et al., 1994). Although we observe individual structures with well-defined wavelengths at shorter scales, we would expect the break toward the dissipative region at smaller scales if the structures were occurring at the bottom side of the OH layer at lower altitudes (Lübken, 1992). Similarly, are we not aware of similar studies for horizontal observations, or for short-scale structures with a well-defined wavelength as presented in this paper. Observational biases in the two techniques, as well as the fact that we are not observing the same

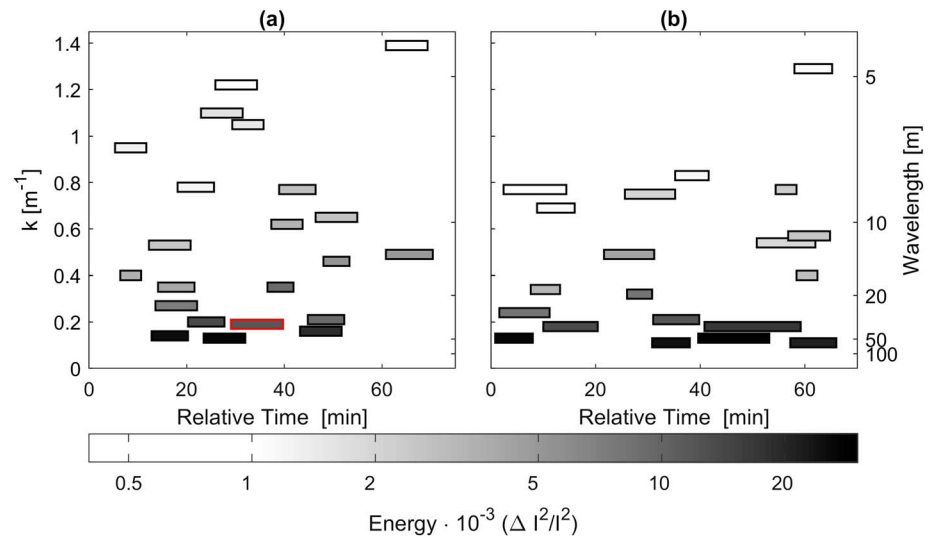


Figure 6. Overview over the 42 quasiperiodic structure (QPS) events detected at their observed wave numbers (wavelengths) and their durations in time. The wave number shown is that projected onto the slit direction. The darkness of each box indicates the energy of the QPS perturbation, with darker shades indicating higher energy. The highest wave number observed during the two nights is 1.39 m^{-1} , which corresponds to a wavelength of 4.5 m. (a) Observations from 21 May 2016. The QPS event from Figure 2 is highlighted in red. (b) Observation from 20 June 2016.

phenomena (random turbulence in the vertical vs. horizontal periodic structures) may account for this apparent discrepancy.

In order to examine whether detector effects could influence the results, we repeated the analysis procedure on the P branch of the OH (9,7) band. The P branch is spread over a wider range of wavelengths as can be seen in Figure 1. As a consequence the P branch is more vulnerable to any leftover detector effects. We again subtracted a linear interpolation of the background. Lines up to $N = 8$ used as higher rotational lines were cut off by the filter. The events presented in Figures 6 and 7 were found in the P

branch as well, after employing the same reduction steps as for the Q branch. Small changes within the statistical noise limits were found in the length, the precise wave number, and the relative energy, and the slope of the energy cascade agreed with that found for the Q branch to within one sigma standard deviation.

To further test that no stray detector signals caused variations along the slit length that would be interpreted as QPS events, the same procedure was repeated for areas between the OH lines where there was no airglow signal. Again, a background on either side was linearly interpolated over the *signal* region and the analysis carried out as described above. With no airglow signal present, no QPS event longer than the Brunt period could be detected. These two tests demonstrate that the results presented above are very small-scale, QPS in the OH airglow and not the result of random fluctuations or localized detector effects.

Finally, we note that the fact that we observe these QPS features implies that either wind speeds are small or the features are not locked to the wind. The latter would be true for turbulent features associated with gravity wave breaking that move with the phase of the parent wave rather than the background wind (Fritts et al., 2003). Thus, depending upon the ground propagation speed of the wave, small-scale structures could remain within the field of view of the telescope for times long enough to be observed. An extreme example would be a breaking mountain wave, where its associated instability structures would be relatively stationary to a ground-based observer.

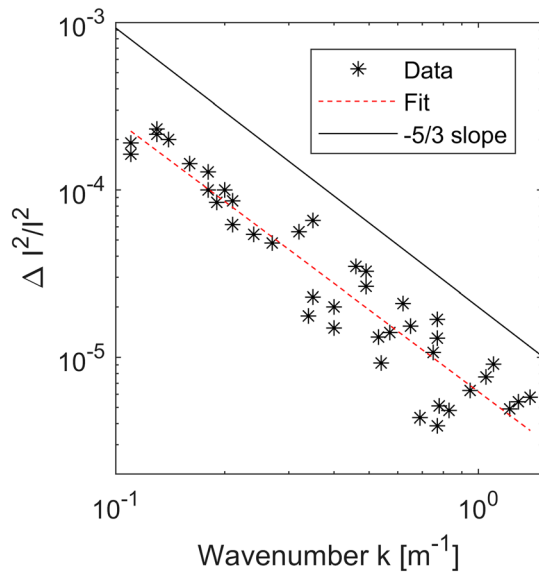


Figure 7. Logarithmic plot of the relative energy in $\Delta I^2/I^2$ versus the wave number of the 42 observed events (stars). A clear correlation of -0.95 is measured. The power-law fit (red, dashed line) yields an exponent of -1.62 ± 0.08 . This suggests that quasiperiodic structures up to a wave number of 1.39 m^{-1} follow the dissipative process of the Kolmogorov cascade model during breaking (shown as a black solid line parallel to the data).

A number of simulations were executed using synthetic data of QPS events with added white noise to verify that the procedure could retrieve wave numbers and energies correctly. This test was executed and recovered the input results for noise levels up to twice those found in the data.

To examine whether sampling the field in one direction distorted the energy spectrum, a number of QPS events with energy and wave number pairs following a Kolmogorov-like $-5/3$ power law were generated with random orientation angles, φ , relative to the slit direction. These were then projected onto the slit, lengthening the wavelengths by a factor of $1/\cos\varphi$. The resulting data were fitted with a power law, as the data presented in Figure 7 above. The resulting exponent in the statistical mean over many simulations is -1.58 ± 0.08 which is within the standard deviation of the measurements presented here and the predicted value of $-5/3$ (-1.67) from the Kolmogorov law. We therefore infer that projecting the wave onto the slit direction does not change the result or our interpretation.

To demonstrate that the projection of the wave onto the slit does not artificially create a power law of $-5/3$, we generated QPS events with completely randomized energies and wave numbers lying in the range of observable energies and wave number of the instrument. We then projected these onto the slit direction and repeated the fit as presented in Figure 7. The resulting energy spectrum shows no correlation or significant relationship between energy and wave number. This indicates that the projection of the waves onto the slit direction cannot artificially create a Kolmogorov-like power law.

4. Conclusion

Three hundred spectra of the (9,7) OH vibrational transition were taken during two nights in May and June 2016 with the NOT in La Palma. The temperature-independent total intensity of the Q branch was calculated for each spectrum. Variations in OH airglow intensity along the slit of the camera showed QPS patterns. The wave numbers and energies of these QPS events were found employing a Lomb-Scargle periodogram. QPS features with wave numbers up to 1.39 m^{-1} could be observed. This wave number corresponds to a wavelength of about 4.5 m.

The consistency over time and the duration of the events were tested and calculated with an autocorrelation function test. The logarithm of the energies and corresponding wave numbers of the QPS events showed a very strong anticorrelation of -0.95 . A least squares fit showed that the two quantities are connected via a power law with an exponent of -1.62 ± 0.08 . This result lies within one sigma of the standard deviation with the predicted value of a Kolmogorov type model. This correspondence indicates that QPS down to scales of 4.5 m horizontal wavelength follow a Kolmogorov-type energy cascade during breaking and that this type of energy cascade model can be used to characterize scales down to 4.5 m in atmospheric gravity wave models.

These results were tested by using the intensity of the P branch instead of the Q branch, which yielded the same results within one sigma standard deviation. However, no QPS longer than at least one Brunt period could be found when employing the method presented here on a spectral area without OH airglow lines. This verifies that the QPS features observed were due to the OH airglow and not associated with position on the detector or stray detector signals.

Acknowledgments

This work was based on observations made with the Nordic Optical Telescope, operated by the Nordic Optical Telescope Scientific Association at the Observatorio del Roque de los Muchachos, La Palma, Spain of the Instituto de Astrofísica de Canarias. We thank the staff from the NOT for their help and support during a visit by C. F. in November 2016. This work was supported by the Research Council of Norway/CoE under contract 223252/F50. Archive data from the NOTCam can be accessed via <http://www.not.iac.es/observing/forms/fitsarchive/> (Nordic Optical Telescope, 2017).

References

- Baker, D. J., & Stair, J. A. T. (1988). Rocket measurements of the altitude distributions of the hydroxyl airglow. *Physica Scripta*, 37(4), 611–622. <https://doi.org/10.1088/0031-8949/37/4/021>
- Becker, E., & Schmitz, G. (2002). Energy deposition and turbulent dissipation owing to gravity waves in the mesosphere. *Journal of the Atmospheric Sciences*, 59(1), 54–68. [https://doi.org/10.1175/1520-0469\(2002\)059<0054:edatdo>2.0.co;2](https://doi.org/10.1175/1520-0469(2002)059<0054:edatdo>2.0.co;2)
- Cot, C. (2001). Equatorial mesoscale wind and temperature fluctuations in the lower atmosphere. *Journal of Geophysical Research*, 106(D2), 1523–1532. <https://doi.org/10.1029/2000JD900597>
- Dewan, E. M., Pendleton, W., Grossbard, N., & Espy, P. (1992). Mesospheric OH airglow temperature fluctuations: A spectral analysis. *Geophysical Research Letters*, 19(6), 597–600. <https://doi.org/10.1029/92GL00391>
- Dietrich, J. C., Nott, G. J., Espy, P. J., Swenson, G. R., Chu, X., Taylor, M. J., et al. (2005). High frequency atmospheric gravity-wave properties using Fe-lidar and OH-imager observations. *Geophysical Research Letters*, 32, L09801. <https://doi.org/10.1029/2004GL021944>
- Djupvik, A. A., & Andersen, J. (2010). The Nordic Optical Telescope. In M. J. Diego, J. L. Goicoechea, I. J. González-Serrano, & J. Gorgas (Eds.), *Highlights of Spanish astrophysics V* (pp. 211–218). Berlin, Heidelberg: Springer.
- Eather, R. H., Mende, S. B., & Judge, R. J. R. (1976). Plasma injection at synchronous orbit and spatial and temporal Auroral morphology. *Journal of Geophysical Research*, 81(16), 2805–2824. <https://doi.org/10.1029/JA081i016p02805>

- Franzen, C., Hibbins, R. E., Espy, P. J., & Djupvik, A. A. (2017). Optimizing hydroxyl airglow retrievals from long-slit astronomical spectroscopic observations. *Atmospheric Measurement Techniques*, *10*(8), 3093–3101. <https://doi.org/10.5194/amt-10-3093-2017>
- Fritts, D. C., & Alexander, M. J. (2003). Gravity wave dynamics and effects in the middle atmosphere. *Reviews of Geophysics*, *41*(1), 1003. <https://doi.org/10.1029/2001RG000106>
- Fritts, D. C., Bizon, C., Werne, J. A., & Meyer, C. K. (2003). Layering accompanying turbulence generation due to shear instability and gravity-wave breaking. *Journal of Geophysical Research*, *108*(D8), 8452. <https://doi.org/10.1029/2002JD002406>
- Fritts, D. C., Laughman, B., Lund, T. S., & Snively, J. B. (2015). Self-acceleration and instability of gravity wave packets: 1. Effects of temporal localization. *Journal of Geophysical Research: Atmospheres*, *120*, 8783–8803. <https://doi.org/10.1002/2015JD023363>
- Fritts, D. C., Wang, L., Baumgarten, G., Miller, A. D., Geller, M. A., Jones, G., et al. (2017). High-resolution observations and modeling of turbulence sources, structures, and intensities in the upper mesosphere. *Journal of Atmospheric and Solar-Terrestrial Physics*, *162*(Supplement C), 57–78. <https://doi.org/10.1016/j.jastp.2016.11.006>
- Hecht, J. H., Liu, A. Z., Walterscheid, R. L., & Rudy, R. J. (2005). Maui mesosphere and lower thermosphere (Maui MALT) observations of the evolution of Kelvin-Helmholtz billows formed near 86 km altitude. *Journal of Geophysical Research*, *110*, D22S10. <https://doi.org/10.1029/2003JD003908>
- Hecht, J. H., Walterscheid, R. L., Fritts, D. C., Isler, J. R., Senft, D. C., Gardner, C. S., et al. (1997). Wave breaking signatures in OH airglow and sodium densities and temperatures: 1. Airglow imaging, Na lidar, and MF radar observations. *Journal of Geophysical Research*, *102*(D6), 6655–6668. <https://doi.org/10.1029/96JD02619>
- Hecht, J. H., Walterscheid, R. L., & Ross, M. N. (1994). First measurements of the two-dimensional horizontal wave number spectrum from CCD images of the nightglow. *Journal of Geophysical Research*, *99*(A6), 11,449–11,460. <https://doi.org/10.1029/94JA00584>
- Hillert, W., Lübken, F. J., & Lehmacher, G. (1994). TOTAL: A rocket-borne instrument for high resolution measurements of neutral air turbulence during DYANA. *Journal of Atmospheric and Terrestrial Physics*, *56*(13-14), 1835–1852. [https://doi.org/10.1016/0021-9169\(94\)90013-2](https://doi.org/10.1016/0021-9169(94)90013-2)
- Holton, J. R. (1982). The role of gravity wave induced drag and diffusion in the momentum budget of the mesosphere. *Journal of the Atmospheric Sciences*, *39*(4), 791–799. [https://doi.org/10.1175/1520-0469\(1982\)039<0791:trogwi>2.0.co;2](https://doi.org/10.1175/1520-0469(1982)039<0791:trogwi>2.0.co;2)
- Holton, J. R. (1983). The influence of gravity wave breaking on the general circulation of the middle atmosphere. *Journal of the Atmospheric Sciences*, *40*(10), 2497–2507. [https://doi.org/10.1175/1520-0469\(1983\)040<2497:tiogwb>2.0.co;2](https://doi.org/10.1175/1520-0469(1983)040<2497:tiogwb>2.0.co;2)
- Humbert, B. K., Gjerloev, J. W., Samara, M., & Michell, R. G. (2017). Scale size-dependent characteristics of the nightside aurora. *Journal of Geophysical Research: Space Physics*, *122*, 147–158. <https://doi.org/10.1002/2016JA023695>
- Kolmogorov, A. N. (1941a). Local structure of turbulence in an incompressible fluid for very large Reynolds numbers. *Comptes rendus (Doklady) de l'Academie des Sciences de l'U.R.S.S.*, *31*, 301–305.
- Kolmogorov, A. N. (1941b). On the degeneration of isotropic turbulence in an incompressible viscous fluid. *Comptes rendus (Doklady) de l'Academie des Sciences de l'U.R.S.S.*, *31*, 538–540.
- Li, F., Liu, A. Z., Swenson, G. R., Hecht, J. H., & Robinson, W. A. (2005). Observations of gravity wave breakdown into ripples associated with dynamical instabilities. *Journal of Geophysical Research*, *110*, D09S11. <https://doi.org/10.1029/2004JD004849>
- Lindzen, R. S. (1981). Turbulence and stress owing to gravity wave and tidal breakdown. *Journal of Geophysical Research*, *86*(C10), 9707–9714. <https://doi.org/10.1029/JC086iC10p09707>
- Liu, A. Z., & Swenson, G. R. (2003). A modeling study of O₂ and OH airglow perturbations induced by atmospheric gravity waves. *Journal of Geophysical Research*, *108*(D4), 4151. <https://doi.org/10.1029/2002JD002474>
- Lomb, N. R. (1976). Least-squares frequency analysis of unequally spaced data. *Astrophysics and Space Science*, *39*(2), 447–462. <https://doi.org/10.1007/bf00648343>
- Lübken, F. J. (1992). On the extraction of turbulent parameters from atmospheric density fluctuations. *Journal of Geophysical Research*, *97*(D18), 20,385–20,395. <https://doi.org/10.1029/92JD01916>
- Lübken, F. J., Hillert, W., Lehmacher, G., von Zahn, U., Blix, T. A., Thrane, E. V., et al. (1994). Morphology and sources of turbulence in the mesosphere during DYANA. *Journal of Atmospheric and Terrestrial Physics*, *56*(13-14), 1809–1833. [https://doi.org/10.1016/0021-9169\(94\)90012-4](https://doi.org/10.1016/0021-9169(94)90012-4)
- Lübken, F. J., Rapp, M., & Hoffmann, P. (2002). Neutral air turbulence and temperatures in the vicinity of polar mesosphere summer echoes. *Journal of Geophysical Research*, *107*(D15), 4273. <https://doi.org/10.1029/2001JD000915>
- Meinel, A. B. (1950a). OH emission bands in the Spectrum of the night sky. I. *The Astrophysical Journal*, *111*, 555–564. <https://doi.org/10.1086/145296>
- Meinel, A. B. (1950b). OH emission bands in the spectrum of the night sky. II. *The Astrophysical Journal*, *112*, 120–130. <https://doi.org/10.1086/145321>
- Müllemann, A., Rapp, M., Lübken, F. J., & Hoffmann, P. (2002). In situ measurements of mesospheric turbulence during spring transition of the Arctic mesosphere. *Geophysical Research Letters*, *29*(10), 1477. <https://doi.org/10.1029/2002GL014841>
- Scargle, J. D. (1982). Studies in astronomical time series analysis. II—Statistical aspects of spectral analysis of unevenly spaced data. *Astrophysical Journal*, *263*, 835–853. <https://doi.org/10.1086/160554>
- Sedlak, R., Hannawald, P., Schmidt, C., Wust, S., & Bittner, M. (2016). High-resolution observations of small-scale gravity waves and turbulence features in the OH airglow layer. *Atmospheric Measurement Techniques*, *9*(12), 5955–5963. <https://doi.org/10.5194/amt-9-5955-2016>
- Staquet, C., & Sommeria, J. (2002). Internal gravity waves: From instabilities to turbulence. *Annual Review of Fluid Mechanics*, *34*(1), 559–593. <https://doi.org/10.1146/annurev.fluid.34.090601.130953>
- Swenson, G. R., & Gardner, C. S. (1998). Analytical models for the responses of the mesospheric OH* and Na layers to atmospheric gravity waves. *Journal of Geophysical Research*, *103*(D6), 6271–6294. <https://doi.org/10.1029/97JD02985>
- Taylor, M. J., Pendleton, W. R. Jr., Pautet, P.-D., Zhao, Y., Olsen, C., Babu, H. K. S., et al. (2007). Recent progress in mesospheric gravity wave studies using nightglow imaging system. *Revista Brasileira de Geofísica*, *25*, 49–58. <https://doi.org/10.1590/S0102-261X2007000600007>
- Thrane, E. V., Blix, T. A., Hoppe, U. P., Lübken, F. J., Hillert, W., Lehmacher, G., et al. (1994). A study of small-scale waves and turbulence in the mesosphere using simultaneous in situ observations of neutral gas and plasma fluctuations. *Journal of Atmospheric and Terrestrial Physics*, *56*(13-14), 1797–1808. [https://doi.org/10.1016/0021-9169\(94\)90011-6](https://doi.org/10.1016/0021-9169(94)90011-6)
- Vetterling, W. T., Teukolsky, S. A., Flannery, B. P., & Press, W. H. (1992). *Numerical recipes in Fortran 77: The art of scientific computing*. New York: Cambridge University Press.